Wireless, battery-free subdermally implantable photometry systems for chronic recording of neural dynamics

Alex Burton[1+], Sofian N. Obaid[2+], Abraham Vazquez-Guardado[3], Matthew B. Schmit[4,5] Tucker Stuart[1], Le Cai[1], Zhiyuan Chen[2], Irawati Kandela[6], Chad R Haney[7], Emily A Waters[7], Haijiang Cai[4,8], John A Rogers[3,9,10,11,12,13,14], Luyao Lu[2]*, Philipp Gutruf[1,8,15]**

[1]Department of Biomedical Engineering, University of Arizona, Tucson, AZ 85721, USA.;
[2]Department of Biomedical Engineering, The George Washington University, Washington, DC 20052, USA.;
[3]Center for Bio-Integrated Electronics, Northwestern University, Evanston, IL 60208, USA.;
[4]Department of Neuroscience, University of Arizona, Tucson, AZ, 85721, USA.;
[5]Graduate Interdisciplinary Program in Neuroscience, University of Arizona, Tucson, AZ, 85721, USA.;
[6]Developmental Therapeutics Core, Northwestern University, Evanston, IL, USA.;
[7]Center for Advanced Molecular Imaging, Radiology, and Biomedical Engineering, Northwestern University, Evanston, IL, USA.;
[8]Bio5 Institute and Department of Neurology, University of Arizona, Tucson, AZ, 85721, USA.;
[9]Feinberg School of Medicine, Northwestern University, Evanston, IL 60208, USA.;
[10]Department of Electrical Engineering and Computer Science, Northwestern University, Evanston, IL 60208, USA.;
[11]Department of Neurological Surgery, Northwestern University, Evanston, IL 60208, USA.;
[12]Department of Chemistry, Northwestern University, Evanston, IL 60208, USA.;
[13]Department of Mechanical Engineering, Northwestern University, Evanston, IL 60208, USA.;
[14]Department of Materials Science and Engineering, Northwestern University, Evanston, IL 60208, USA.;
[15]Department of Electrical and Computer Engineering, University of Arizona, Tucson, AZ 85721, USA.;

[+]Authors contributed equally

** Co-Corresponding authors*

www.pnas.org/cgi/doi/10.1073/pnas.1920073117

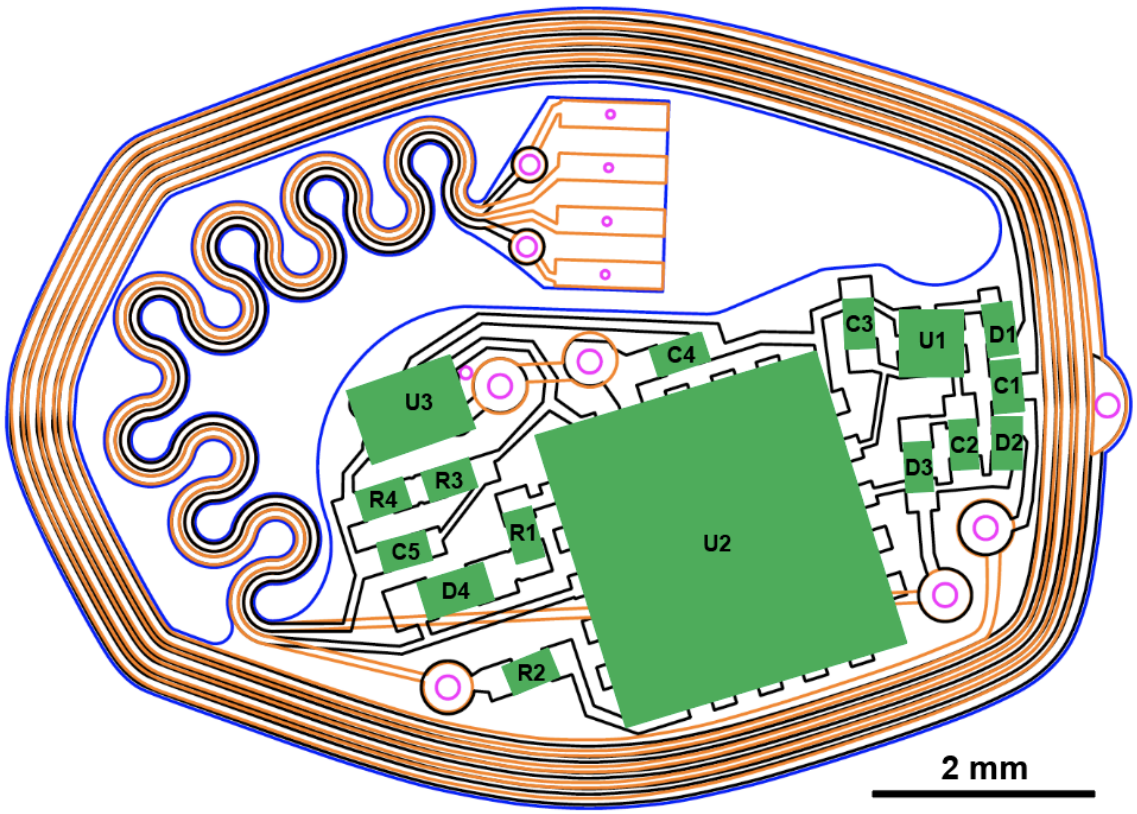

C1	~50-150 pF, Based on Device Tuning
C2	2.2 µF ±10%, 50 V
C3	2.2 µF ±10%, 50 V
C4	2.2 µF ±10%, 50 V
C5	20 pF ±5%, 50 V

R1	1 kΩ ±1%
R2	1 kΩ ±1%
R3	18 MΩ ±1%
R4	18 MΩ ±1%

D1	Diode Schottky 40 V
D2	Diode Schottky 40 V
D3	Diode Zener40 V
D4	IR LED 480 nm

U1	3.3 V LDO, 250 mA - 4WLCSP
U2	Attiny 84 - 20QFN
U3	ADA4505-1 – 6WLCSP

Figure S1. Device design with the layout of the electrical components (green) and a list of corresponding components listed below. Tuning capacitors of 79 pF are used on the large coil and a 120 pF for the small coil.

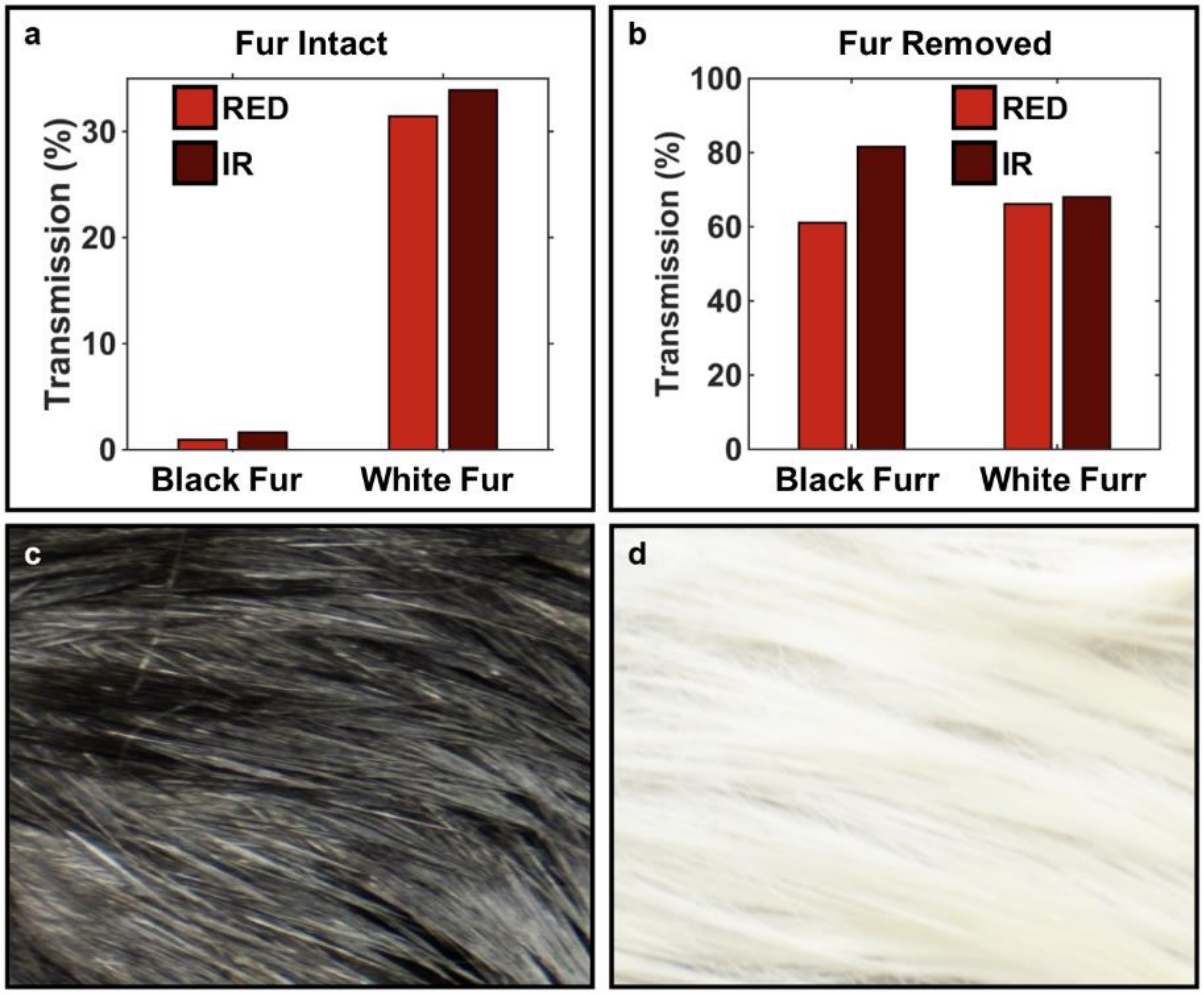

Figure S2. Optical characterization of mouse scalp. (a) Transmission measurements of black fur mouse (C57BL/6) and white fur mouse strain (Swiss Webster) with intact fur in transmission (SMD LED light source behind scalp; Red: 624 nm IR: 950 nm). (b) Transmission measurement with shaven scalp. (c) Photographic image of the black fur (C57BL/6). (d) Photographic image of the white fur (Swiss Webster).

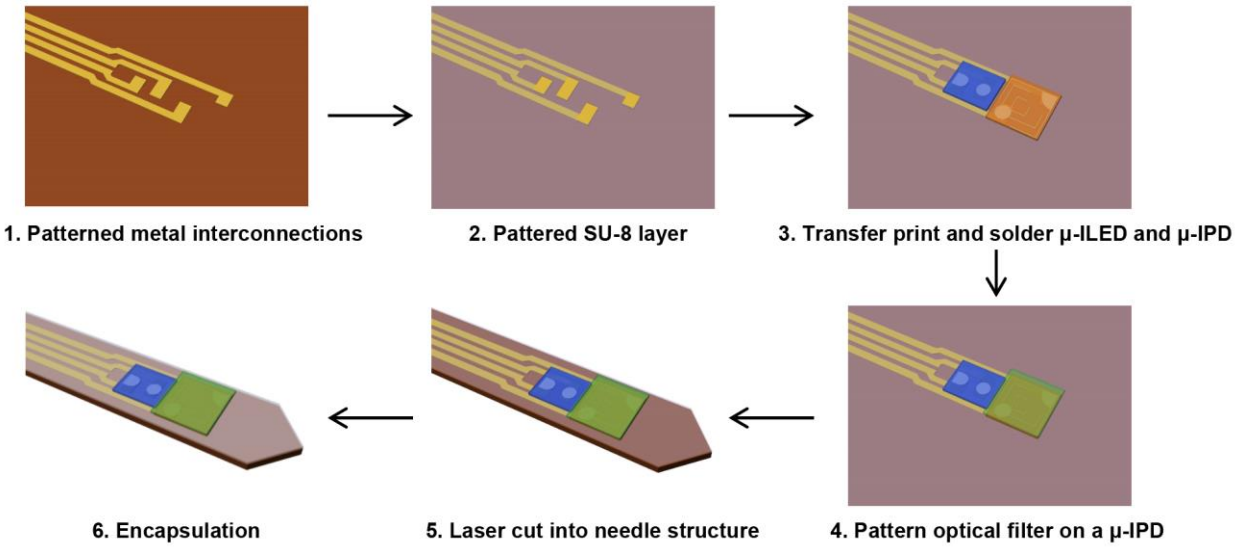

Figure S3. Schematic illustration of key fabrication steps for a wireless, injectable photometry probe.

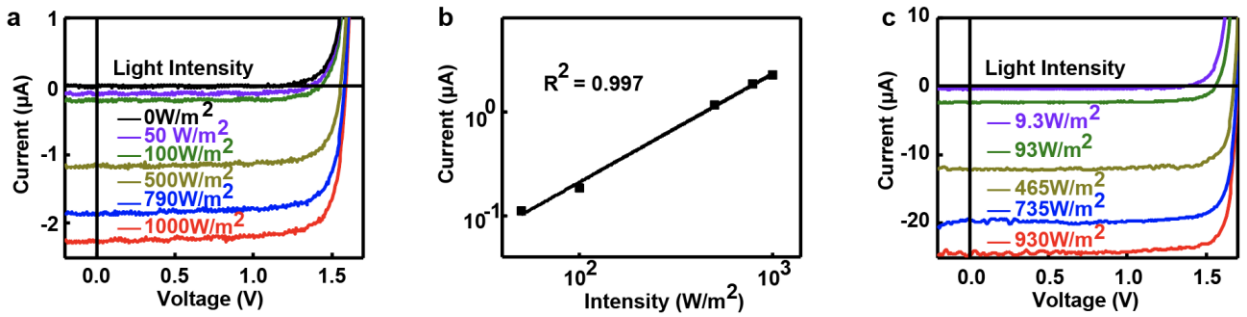

Figure S4. (a) Light intensity-dependent current-voltage characteristics of the μ-IPD under simulated solar illumination. Red, blue, dark yellow, olive, violet, and black represent the light intensity of 1000, 790, 500, 100, and 50 W/m^2 and the dark condition, respectively. **(b)** Light intensity-dependent I_{sc} of the μ-IPD under simulated solar illumination. **(c)** Light intensity-dependent current-voltage characteristics of the μ-IPD under green LED illumination. Red, blue, dark yellow, olive, violet, and black represent the light intensity of 930, 735, 465, 93, and 9.3 W/m^2.

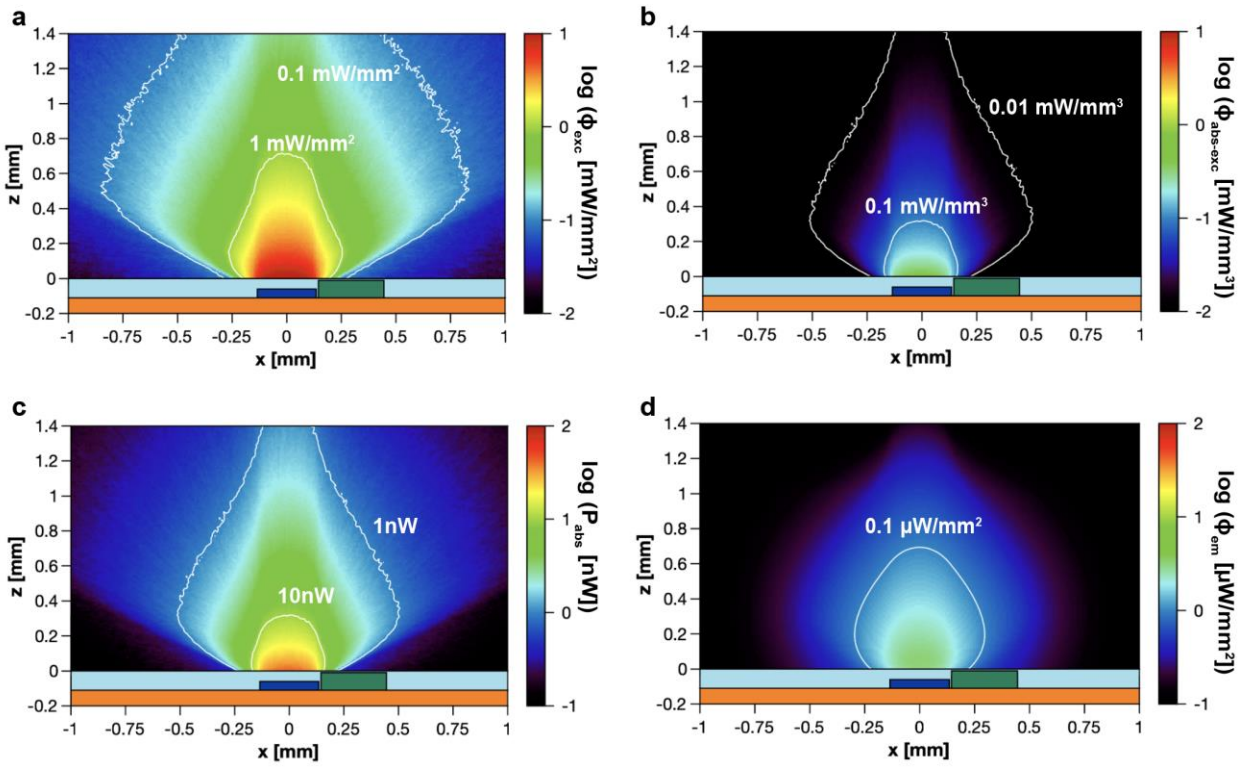

Figure S5. (a) Simulation of the illumination fluence profile created from the µ-ILED. **(b)** Absorbed power density, and **(c)** total absorbed power by fluorescent molecule at 470 nm. **(d)** Fluorescence fluence at 0.06 µM Ca^{2+} concentration.

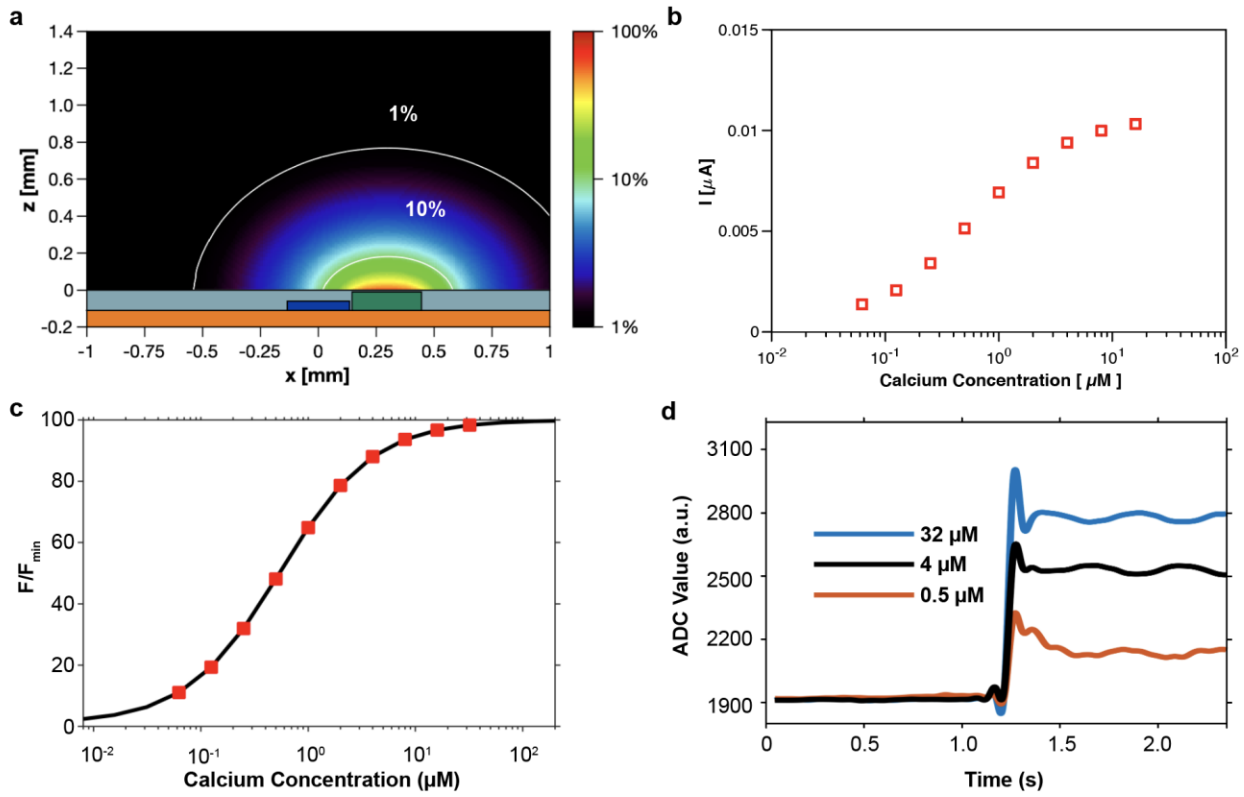

Figure S6. (a) Photodetector acceptance in aqueous solution without the thin film optical filter. **(b)** Relative fluorescence as a function of Ca^{2+} concentration. **(c)** Estimated photodetector current based on Monte Carlo simulation. **(d)** ADC recording of the device as it is being inserted in 3 separate Ca^{2+} concentrated solutions.

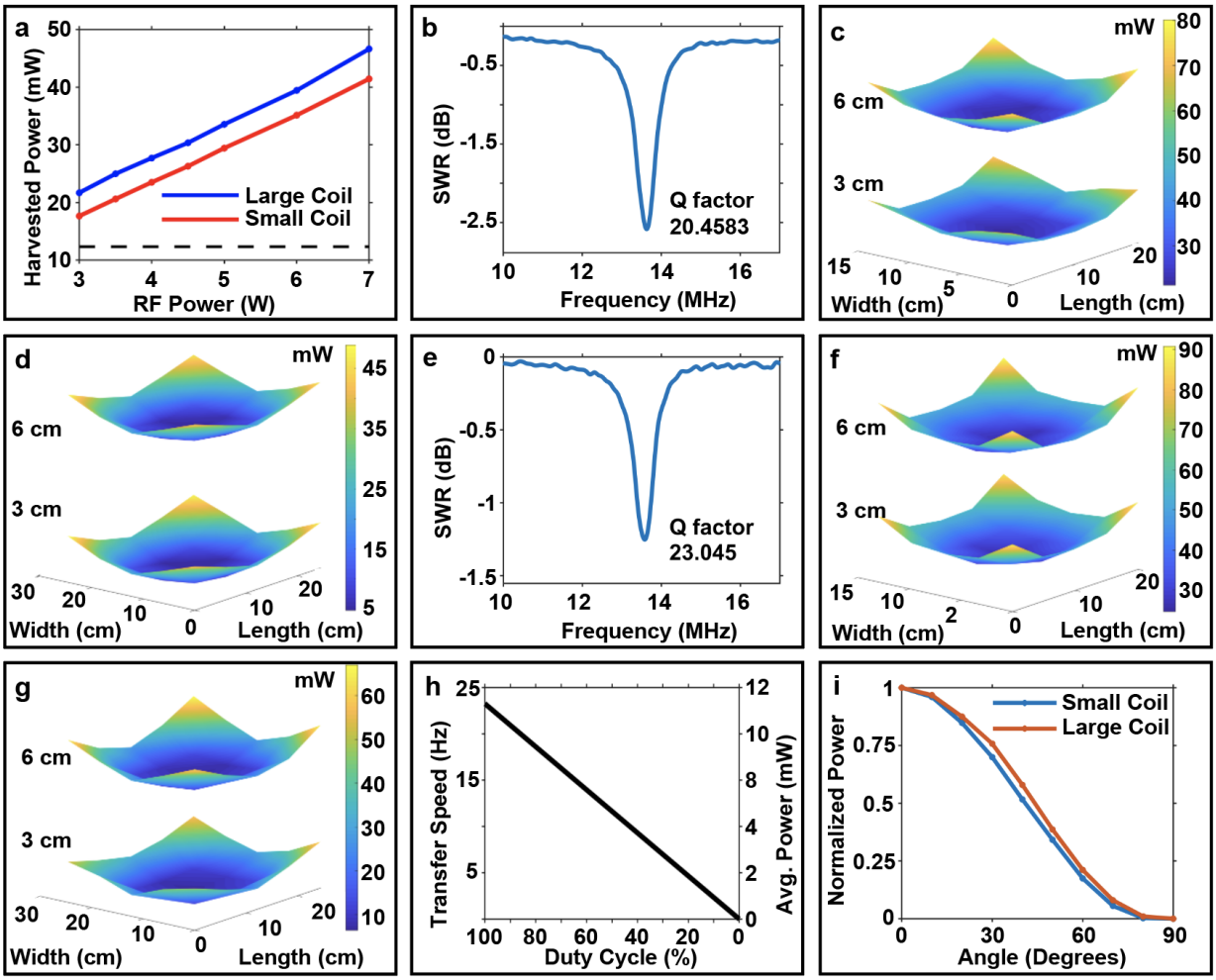

Figure S7. (a) Mice home cage (18 cm x 12 cm) powering both the large and small photometry device. **(b)** SWR of the small photometry device. **(c)** Energy harvesting capability of the smaller device in a 2 turn primary coil cage with 18 cm x 12 cm dimension with 5 W RF power. **(d)** Energy harvesting capability of the smaller device in a 2 turn primary coil cage with 25.5 cm x 25.5 cm dimensions with 5 W RF power. **(e)** SWR of the larger photometry device. **(f)** Energy harvesting capability of the larger device in a 2 turn primary coil cage with 18 cm x 12 cm dimensions with 5 W RF power. **(g)** Energy harvesting capability of the larger device in a 2 turn primary coil cage with 25.5 cm x 25.5 cm dimensions with 5 W RF power. **(h)** Power consumption vs Duty Cycle. **(i)** Normalized power harvested based on angular misalignment of the device relative to the primary coil.

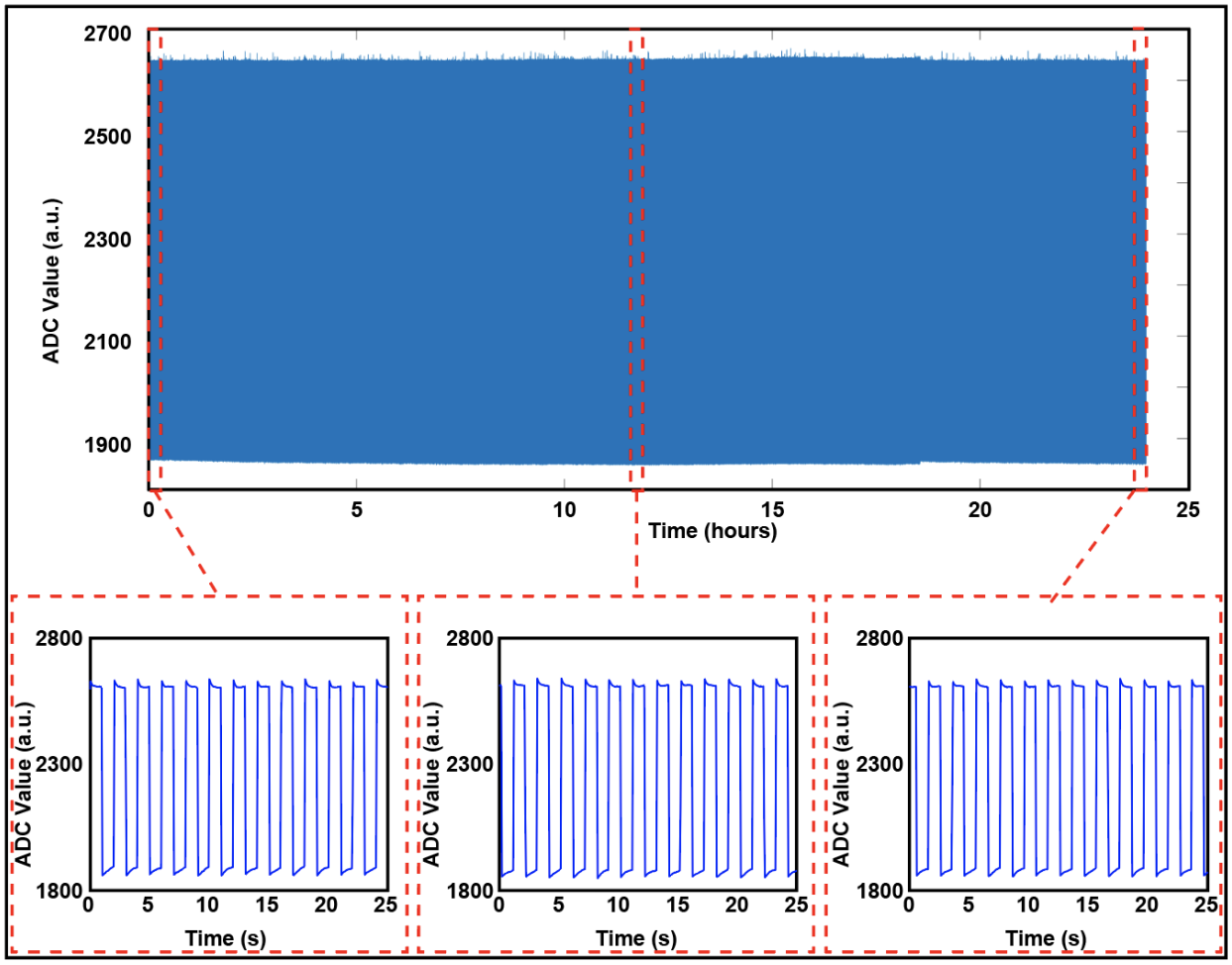

Figure S8. 24-hour benchtop recording of an external green light source (520 nm) within a mice home cage at input power of 3 W with insets showing segments of the recorded green light source pulsing at 1 second intervals.

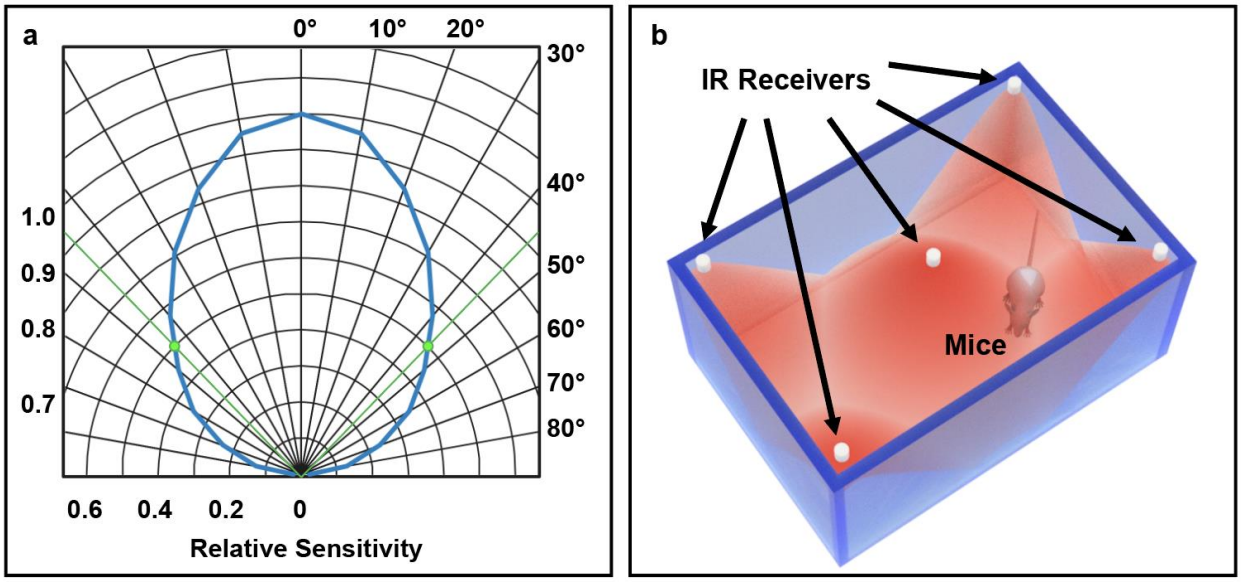

Figure S9. (a) Relative sensitivity of the IR receiver based on angular positioning of the transmitter with half relative sensitivity marked at 45° (green). **(b)** 3D rendering of a mice in a 30 cm x 20 cm cage with 5 IR receivers at the top of the cage with red field of view cones indicating the half sensitivity of the IR receivers.

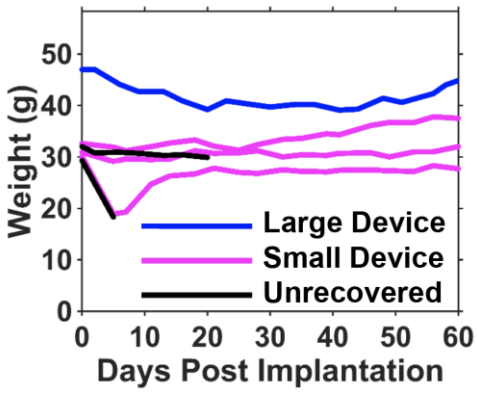

Figure S10. Average body weight of the mice (n=6) post-surgery with either the large (blue) and small (pink) devices implanted. One mouse from the larger device survived for 20 days and one mouse with the smaller device survived for 5 days post-surgery.

Text ST1. The optical fluence was calculated using Monte Carlo simulations in aqueous solution in a numerical volume of 301 x 301 x 250 bins, each with 1 x 10^{-9} cm^3 volume (RS1). The absorption coefficient of the solution was dominated by the fluorescent molecule homogenously dispersed. Oregon Green BAPTA-2 (OGB-2) has a molar absorption coefficient of $\varepsilon_{OGB\text{-}2}$ = 76,000 cm^{-1} M^{-1} at 490 nm (40% at 470 nm). At a test concentration of 12.5 μM and μ-ILED center emission wavelength of 470 nm, the absorption coefficient is $\mu_{a\text{-}OGB\text{-}2}$ = 0.38 cm^{-1}. The scattering coefficient was set at 10 cm^{-1}. A dissymmetry factor g = 0.85 accounts for mostly forward scattering.

Fig. S4a shows the fluence cross section of a blue LED ϕ_{exc} (**r**) [mW/cm^2], where **r** is the position vector. The wavelength and optical power are 470 nm and 0.5 mW, respectively. The excitation photon fluence is absorbed by the fluorescent molecule. The absorption density profile is proportional to both excitation fluence and absorption coefficient, $P_{exc\text{-}abs} = \phi_{exc}\ \mu_{a\text{-}OGB\text{-}2}$ [mW/cm^3], and provides an estimate of the absorbed power per unit volume, see Fig. S4b. The total absorbed power was calculated by means of the known numerical bin volume used in the simulation, $P_{abs} = \phi_{exc}\ \mu_{a\text{-}OGB\text{-}2}\ V_{bin}$ [mW], see Fig S4c, and is the amount of power involved in fluorescent energy transfer.

The fluorescent molecule OGB-2 has a dissociation constant of K_d = 0.55 μM, and it has a large fluorescent intensity contrast in the presence of calcium (F_{max}) with respect to calcium-free (F_{min}) states, F_{max} / F_{min} = ~100, according to its datasheet. The calcium concentration is estimated using the following calibration curve as a function of fluorescence (F) (RS2).

$$[Ca^{2+}] = K_d \frac{F - F_{min}}{F_{max} - F} \quad (1)$$

The relative fluorescence can be calculated by solving for F in Eq. 1 and expressed as a function of calcium concentration.

$$F = F_{\min} \frac{(\sim 100)\frac{[Ca^{2+}]}{K_d}+1}{\frac{[Ca^{2+}]}{K_d}+1} \frac{F-F_{min}}{F_{max}-F} \quad (2)$$

The scope of Eq. 2 depends on many parameters, from quality of reagent and test solutions, to the fluorescence measuring system parameters such as detector sensitivity. Thus, experimental characterization is needed to determine the dynamic range of the assay with respect to the measurement apparatus, which fixes the power range of detected fluorescence. Nevertheless, the fluorescence signal qualitatively follows according to Eq. 2 as seen in Fig. S5c. In the simulations the lower limit of fluorescence was set at $F_{min} = 0.01$.

The fluorescence fluence, $\phi_{em}(\mathbf{r})$ [W/cm^2] was calculated using a test fluorescent point source, with photon fluence $\phi_{em0}(\mathbf{r}')$ [cm^{-2}], where $\mathbf{r}'$ is the position vector of the test point source, with emission wavelength at 523 nm (RS3). At this wavelength, both water and OGB-2 have negligible absorption (~0.004 cm^{-1}) and low scattering coefficient (~1 cm^{-1}), and g = 0.85. The numerical simulation volume and bin size were the same as in the case for illumination. This test point source emits a fluorescent power according to the total absorbed excitation power $P_{exc\text{-}abs}(\mathbf{r}')$, the quantum yield Q = 0.7, as well as the concentration of calcium that determines the strength of the emitted fluorescence power (Eq. 2). The total fluorescence fluence at a particular point of interest, given by the following equation, is non-local and depends on the collective emitted fluorescence fluence at other points in space (S3, S4).

$$\phi_{em}(\boldsymbol{r}) = F([Ca^{2+}])Q \sum_{r=V} [P_{\text{abs}}(\text{r} - \text{r}')\phi_{em0}(r - r')] \frac{F-F_{min}}{F_{max}-F} \quad (3)$$

The photocurrent baseline was calculated by the addition of blue light transmission of 0.2 μW through the optical filter, resulting in 11.29 nA photocurrent. Furthermore, edge coupling of blue light into the photodetector is calculated to be 0.97 μW, which contributes to 37.65 nA of photocurrent. These contributions combine to yield 48.94 nA of baseline current.

The photodetector acceptance was calculated using a test point source emitting 1 mW of power at 523 nm in aqueous solution following the same Monte-Carlo method and parameters described previously. This test point source was swept across the superstrate volume. At each point in space, the received power at the photodetector was calculated and normalized with the power of the point source, to yield the spatial distribution of the detection efficiency with and without the optical filter. See Fig. 2i and Fig. S5a respectively.

Text ST2. Mice were anesthetized in an induction chamber with 3% isoflurane in oxygen and transferred to a dedicated imaging bed with isoflurane delivered via nosecone at 1-2%. For both imaging systems, a separate mouse bed was used. Mice were placed in the prone position with the head immobilized with ear and tooth bars.

During μCT imaging, respiratory signals were continuously monitored using a digital system (Mediso-USA, Boston, MA). Images of the mice were acquired with a preclinical microPET/CT imaging system, (Mediso nanoScan scanner). Data were acquired with 2.17 magnification, 33 μm focal spot, 1 x 1 binning, with 720 projections over a full circle, with a exposure time of 300 ms. Images were acquired, using a peak tube voltage of 35 - 70 kV. Each projection was reconstructed with a voxel size of 68 μm while using a butterworth filter back-projection software from Mediso.

MRI images were taken on a 9.4 T Bruker Bio spec MRI system with a 30 cm bore and a 12 cm gradient insert (Bruker Biospin Inc, Billerica, MA). Respiratory signals were continuously monitored using a MR-compatible system (SA Instruments, Stonybrook, NY) with warm circuiting pads to maintain the animal's body temperature. The actively decoupled 4-channel receiver coil (Bruker Biospin, Inc, Billerica, MA) was mounted to the mice platform which is placed inside a 72 mm quadrature volume coil in transmit-only mode (Bruker Biospin, Inc, Billerica, MA). Images were collected using an accelerated spin echo sequences (Turbo Rapid Acquisition with Relaxation Enhancement, TurboRARE) that are oriented in the axial, sagittal, and coronal directions. The following parameters are used for each MRI scan: TR/TE = 1250 ms / 21.3 ms, RARE factor 8, MTX = 256 x 256, FOV 3 x 3 cm, 7 - 13 slices of 0.75 - 1 mm thick, flip back enabled, and 3 signal averages with a total acquisition time of ~2 mins per scan. Data reconstruction was visualized using Amira 6.7 (FEI, Houston, TX) allowing both MRI and

μCT images to be manually superimposed over one another. Further processing using Amira was used to reduce image artifacts in the CT images using non-local means filtering.

References

RS1. L. Wang, S. L. Jacques, L. Zheng, MCML—Monte Carlo modeling of light transport in multi-layered tissues. *Comput. Methods Programs Biomed.* **47**, 131–146 (1995).

RS2. G. Grynkiewicz, M. Poenie, R. Y. Tsien, A new generation of Ca2+ indicators with greatly improved fluorescence properties. *J. Biol. Chem.* **260**, 3440–3450 (1985).

RS3. A. Liebert, H. Wabnitz, N. Żołek, R. Macdonald, Monte Carlo algorithm for efficient simulation of time-resolved fluorescence in layered turbid media. *Opt. Express* **16**, 13188–13202 (2008).

RS4. M. Keijzer, R. R. Richards-Kortum, S. L. Jacques, M. S. Feld, Fluorescence spectroscopy of turbid media: Autofluorescence of the human aorta. *Appl. Opt.* **28**, 4286–4292 (1989).